

Cite this: *Sustainable Energy Fuels*,  
2025, 9, 6822

# Evolution of the sulfur strand length distribution in lithium organo-sulfur batteries monitored through operando X-ray absorption spectrometry

Konstantin Skudler,<sup>1</sup> Rukiya Matsidik,<sup>2</sup> Ayda Gholamhosseinian,<sup>3</sup>  
Hongfei Yang,<sup>4</sup> Michael Walter,<sup>5</sup> Michael Sommer<sup>6</sup>  
and Matthias Müller<sup>7</sup>Received 18th August 2025  
Accepted 30th October 2025

DOI: 10.1039/d5se01115a

rsc.li/sustainable-energy

Recently, it has been shown that the sulfur load and subsequently the sulfur strand length of organo-sulfur networks prepared *via* inverse vulcanization for lithium organo-sulfur batteries impact the battery performance in terms of specific capacity and stability. In this work, we quantify the distribution of sulfur strand lengths evolving over the course of several charge–discharge cycles using operando X-ray absorption spectrometry. The results correlate the stability of sulfur strand length and (ir)reversibility of S-strand reduction and accompanied cleavage with battery cycling.

## 1 Introduction

As an alternative energy storage technology to lithium-ion batteries, lithium–sulfur (Li–S) batteries have attracted researchers' attention since the invention of their prototype in the early 1960s,<sup>1</sup> due to the abundance of raw materials, competitive cost and significantly high theoretical specific capacity.<sup>2</sup> Based on current studies, the main barrier hindering the Li–S battery system from achieving long-term stability and thus widespread commercialization is the polysulfide shuttle effect.<sup>3</sup> Resulting from the nature of the sulfur redox reaction, by which the intermediate products, lithium polysulfides, are soluble in most of the organic electrolytes and travel with solvents, the active material gets lost, thus leading to capacity fading.<sup>4</sup> There are many research branches aimed at solving this problem by targeting various components of the battery system,<sup>5,6</sup> for instance a functionalized separator suppressing shuttling<sup>7–10</sup> or advanced variations of the electrolyte and the cathodic structure to mitigate the creation and solubility of lithium polysulfides.<sup>11–15</sup>

Organic batteries offer an opportunity to enhance the stability of the cathodic structure. However, their low specific capacity limits their practical application.<sup>16–18</sup> Organo-sulfur

batteries combine the structural integrity of organic frameworks with the high theoretical capacity of sulfur, aiming to bridge the gap between stability and specific capacity.

We have recently reported organo-sulfur polymer networks ( $S_n\text{NDI}_y$ ), in which a monomer based on naphthalene diimide (NDI) is copolymerized with octasulfur ( $S_8$ ) *via* inverse vulcanization.  $S_n\text{NDI}_y$  networks with varying sulfur strands could be synthesized by tuning the feed ratio of sulfur and the monomer.<sup>19</sup> The resulting distribution of sulfur strand lengths impacts the cathodic structure and thus the electrochemical performance of the battery.

Batteries with shorter sulfur strand lengths showed superior cycling stability because the S–C bond has been shown to be more stable than the neighboring S–S bond.<sup>20–23</sup> However, single sulfur atom bridges enable polymerization, but do not contribute to the batteries' capacity. The question arises as to which sulfur strand lengths make the organo-sulfur cathode stable during cycling while maintaining the highest possible specific capacity.

Near-Edge X-ray Absorption Fine Structure (NEXAFS) spectroscopy, a technique sensitive to the local electronic structure and chemical environment of specific elements,<sup>24</sup> enables the investigation of the correlation between the electrochemical performance of a battery and its corresponding network structure. Employing model spectra and considering the influence from the self-absorption effect, the distribution of sulfur strand lengths in different cathode materials can be determined quantitatively.<sup>25</sup>

Building upon this approach, operando NEXAFS allows the method to be applied to half-cells during cycling. An operando approach provides the opportunity to reveal the evolution of the sulfur strand length distribution within a single cycle or over a period of multiple charge–discharge cycles. Understanding

<sup>1</sup>Physikalisch-Technische Bundesanstalt (PTB), Abbestr. 2–12, 10587 Berlin, Germany. E-mail: Konstantin.Skudler@ptb.de; Matthias.Mueller@ptb.de

<sup>2</sup>Institute for Chemistry, Chemnitz University of Technology, Str. der Nationen 62, 09111 Chemnitz, Germany

<sup>3</sup>Freiburg Center for Interactive Materials and Bioinspired Technologies (FIT), University of Freiburg, Georges-Köhler-Allee 105, 79110 Freiburg, Germany

<sup>4</sup>Cluster of Excellence LiMatS @ FIT, Freiburg, Germany

<sup>5</sup>Fraunhofer IWM, MikroTribologie Centrum  $\mu\text{TC}$ , Freiburg, Germany

<sup>6</sup>Forschungszentrum MAIN, Chemnitz University of Technology, Rosenbergstraße 6, 09126 Chemnitz, Germany



the correlation between structural and electrochemical properties is the key to developing lithium–sulfur batteries with both high capacity and long cycle stability.

This work includes operando results of  $\text{Li-S}_n\text{NDI}_y$  battery half-cells consisting of cyclic voltammograms and NEXAFS spectra. The extracted evolution of the sulfur strand length distribution over several cycles reflects the cycling stability of the different structural units and thereby offers molecular-level insights into the organo-sulfur battery system.

## 2 Experimental setup, methods and materials

### 2.1 Sample preparation

The  $\text{S}_n\text{NDI}_y$  polymer networks, cathodes and half-cells were prepared as described previously.<sup>19</sup> In the synthesis, (100 –  $y$ ) wt% sulfur and  $y$  wt%  $N,N'$ -bis(2-propenyl)-1,4,5,8-naphthalenetetracarboxylic diimide (NDI-pro) react in inverse vulcanization to build an organo-sulfur polymer network. The molar ratio of incorporated sulfur and NDI results in the stoichiometric sulfur strand length  $n$ . This represents the number of atoms per sulfur strand, assuming a uniform distribution within the network and full conversion of all cross-linker sites. As investigated previously,<sup>25</sup> these assumptions do not hold, and sulfur strands follow a broad distribution, also towards longer chains. This causes the polymer networks to include sulfur strands longer than  $n$ .

Synthesized polymer network samples  $\text{S}_1\text{NDI}_{85}$  and  $\text{S}_2\text{NDI}_{72}$  with NDI-pro weight ratio percentages of  $y = 85$  and  $y = 72$  have resulting stoichiometric sulfur strand lengths of  $n = 1$  and  $n = 2$ , respectively. The corresponding cathodes contain 76 wt% of the respective polymer networks, 19 wt% of multi-walled carbon nanotubes (MWCNT) as an additive and 5 wt% of poly(vinylidene fluoride) (PVDF) as a binder. These cathode slurries in  $N$ -methyl-2-pyrrolidone (NMP) were coated onto a nickel mesh, and the cathodes had S-NDI loadings of 3.5 mg ( $\text{S}_1\text{NDI}_{85}$ ) and 3.2 mg ( $\text{S}_2\text{NDI}_{72}$ ), respectively. Together with lithium metal anodes and 100  $\mu\text{l}$  of 2.0 M bis(trifluoromethane)sulfonimide lithium salt (LiTFSI) and 0.25 M lithium nitrate ( $\text{LiNO}_3$ ) in 1,3-dioxolane/1,2-dimethoxyethane (DOL/DME) electrolyte,  $\text{Li-S}_n\text{NDI}_y$  half-cells were assembled in coin cell housings which are further described in Section 2.2.

The NEXAFS spectra of the molecules dipropyl sulfide (DPS), dipropyl disulfide (DPDS) and dimethyl disulfide (DMTS) are used in the basis set for the linear combination analysis of the spectra.<sup>26</sup> Fig. 1 illustrates the  $\text{S}_n\text{NDI}_y$  polymer network and the chemical structure of the organo-sulfur molecules.

### 2.2 NEXAFS measurements

NEXAFS spectra were measured at the Four Crystal Monochromator (FCM) beamline in the PTB laboratory at BESSY II using Si (111) crystals.<sup>27</sup> The exciting X-ray beam reached the cathode through a 4  $\mu\text{m}$  thick highly oriented pyrolytic graphite (HOPG) window covering a hole in the coin cell housing with a diameter of 2 mm. The NEXAFS signal was detected in fluorescence mode using an energy-dispersive silicon drift detector

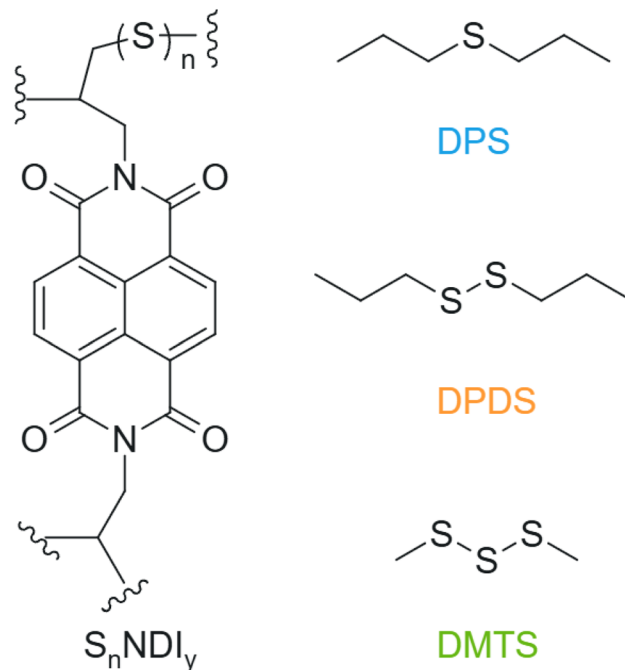


Fig. 1 Chemical structure of the  $\text{S}_n\text{NDI}_y$  polymer network and the model molecules dipropyl sulfide (DPS), dipropyl disulfide (DPDS) and dimethyl trisulfide (DMTS) used as basis spectra for fitting.

(SDD) which was positioned at an angle of  $60^\circ$  relative to the incoming beam. Both the incoming and the detected radiation form an angle of  $30^\circ$  with the sample normal. The measurements were done at the sulfur absorption K-edge with the typical S–S peak located at an incident X-ray energy of 2472.1 eV. All NEXAFS spectra are normalized to fluorescence count rates well above the absorption edge.

In the operando measurements, NEXAFS spectra were taken continuously during cyclic voltammetry (CV) of the batteries. A voltage scan rate of  $0.1 \text{ mV s}^{-1}$  was chosen such that one charge–discharge cycle takes approximately 7 hours. Recording one NEXAFS spectrum takes approximately ten minutes. Multiple measurements were performed before cycling to verify that the cathodic spectra are reproducible. There is no indication of significant beam damage in the electrolyte signal after cycling, as shown in Fig. 2.

### 2.3 Data evaluation

The sulfur strand length distribution is determined by a linear combination analysis of a NEXAFS spectrum taking the self-absorption effect into account.<sup>25</sup> The basis spectra for fitting were taken from highly diluted DPS, DPDS and DMTS samples, representing mono- ( $\text{S}_1$ ), di- ( $\text{S}_2$ ) and trisulfide ( $\text{S}_3$ ) linkages, in fluorescence mode with negligible self-absorption.<sup>26</sup> An additional peak is added to the basis set as a signature of lithium sulfur (LiS) bonds. While these bonds may occur at any site in the cathode, the energy position of the LiS peak is taken from that typical of lithium polysulfides at around 2470 eV.<sup>15,28,29</sup> A linear combination is formed depending on the coefficients representing the molar fractions of the different sulfur species.



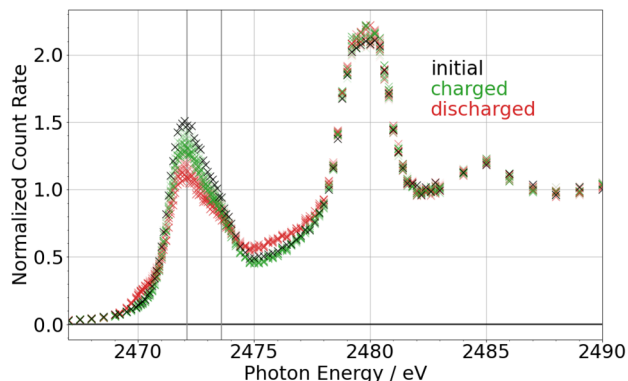


Fig. 2 NEXAFS spectra of the Li-S<sub>2</sub>NDI<sub>72</sub> half-cell in the initial (black) and all discharged (red) and charged (green) states. There is no indication of significant beam damage in the electrolyte signal after cycling. Guiding lines at 2472.1 eV and 2473.6 eV indicate the resonance energies of DPDS in all figures showing NEXAFS spectra.

With a calculation of the self-absorption effect, this parametrized spectrum is fitted to the experimental data, which builds a self-absorption corrected evaluation of the NEXAFS spectra.<sup>30</sup>

Since the basis component with the additional peak is not a full spectrum, the LiS coefficient is only proportional but not equal to the molar fraction. Hence, it cannot be compared to the molar fractions of the other species on an absolute scale. However, they are correlated with each other through the state of charge during cycling.

The energy range for the fitting routine is limited to energies below 2474.5 eV. This range includes the characteristic spectral shape of the different organo-sulfur linkages as well as LiS bonds, but does not require further basis spectra of other sulfur species. Other sulfur species present in the battery cells (mainly oxidized sulfur in the electrolyte, but also lithium monosulfide and potentially products of beam damage) have resonances at

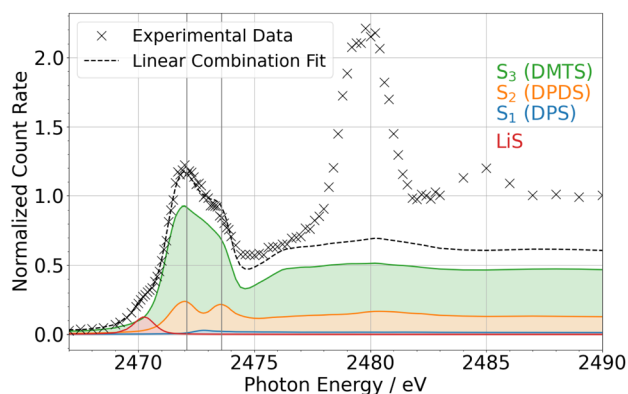


Fig. 3 NEXAFS spectrum of the Li-S<sub>2</sub>NDI<sub>72</sub> half-cell in a discharged state shown as an example. The linear combination (dashed line) consisting of DPS (blue), DPDS (orange) and DMTS (green), representing S<sub>1</sub>, S<sub>2</sub> and S<sub>3</sub> components, respectively, as well as the additional peak of lithium sulfur bonds (LiS, red), resembles the experimental data (crosses) within the fitting energy range up to 2474.5 eV. Resonances at higher energies originate from oxidized sulfur species mainly in the electrolyte and are therefore not considered further.

higher excitation energies. Therefore, the absolute signal in certain regions of the normalized NEXAFS spectra depends on the molar fraction of certain sulfur species in the whole sample.

The self-absorption correction in the selected energy range is only valid when contributions from other sulfur species, including their edge jumps, are negligible. Therefore, the parametrized spectrum (dashed line in Fig. 3) only includes sulfur species with resonances in this specific energy range. After the self-absorption effect has been calculated, the spectrum is renormalized to match the experimental spectrum (crosses in Fig. 3), which contains signals from all sulfur species. The resulting renormalized coefficients can then be interpreted as the molar fractions of the respective sulfur species in the sample. The renormalization factor is a free fitting parameter.

## 2.4 Computational settings

The NEXAFS spectra of sulfur interacting with lithium cannot be measured directly, so we have used simulations. These were based on density functional theory (DFT) with the transition-potential (TP) method as implemented in the GPAW package<sup>31–33</sup> closely following our previous investigation of S K-edge NEXAFS spectra.<sup>34</sup> In brief, the exchange–correlation potential is approximated using Perdew–Burke–Ernzerhof (PBE),<sup>35</sup> a real space grid with a spacing of  $h = 0.2 \text{ \AA}$  was used to represent the Kohn–Sham states, and the simulation box was ensured to extend at least  $4 \text{ \AA}$  around each atom. A maximal force criterion of  $0.05 \text{ eV \AA}^{-1}$  was applied in structure relaxations. The molecules are treated in a DOL/DME solvent environment represented by an implicit solvent<sup>36</sup> with relative permittivity of  $\epsilon_r = 7.27$ .<sup>37</sup>

The X-ray absorption spectra were converted to the absolute energy scale through  $\Delta$ -Kohn–Sham calculations<sup>38</sup> including a semi-empirical energy correction for S (1s) core-excitations from ref. 34 for spin-polarized calculations. The dipole matrix elements were calculated using the transition potential method as detailed in ref. 39. The intensities are obtained as folded oscillator strengths (FOS) with units of  $1/\text{eV}$  that were convoluted by Lorentzians with a full width at half maximum of  $2\gamma = 1.1 \text{ eV}$ .

## 3 Results

### 3.1 Electrochemical performance

The electrochemical performance of the operando Li-S<sub>1</sub>NDI<sub>85</sub> and Li-S<sub>2</sub>NDI<sub>72</sub> half-cells was investigated with cyclic voltammetry (CV) to observe and identify the potentials of electrochemical activity. Similar CV curves of a representative cycle after stabilization of Li-S<sub>n</sub>NDI<sub>y</sub> half-cells with regular coin cells without a window have been published by Matsidik *et al.*<sup>19</sup> The similarities confirm that the HOPG window does not significantly affect the electrochemical behaviour of the batteries and that the fabrication of the cells is sufficiently reproducible. The cyclic voltammograms for the first 8 cycles are shown in Fig. 4.

The first CV cycle of S<sub>1</sub>NDI<sub>85</sub> shows a double redox pair with charging peaks at 2.5 V and 2.7 V and discharging peaks at 2.3 V



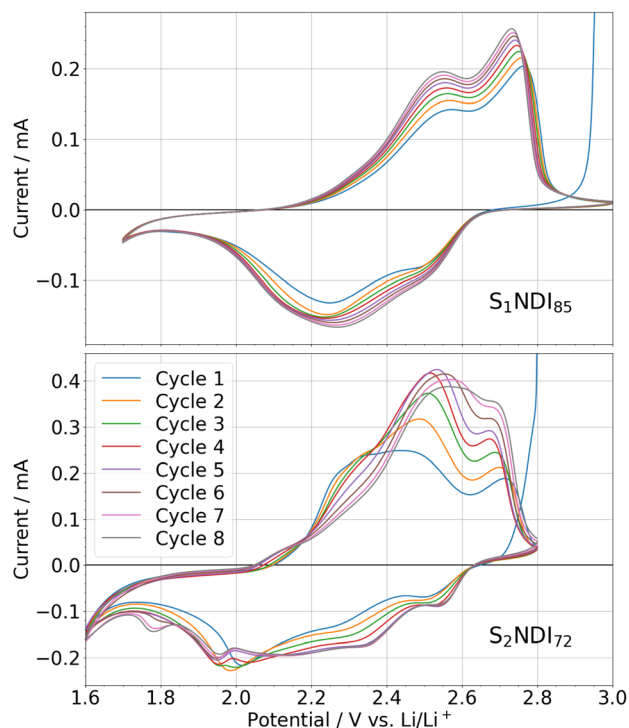


Fig. 4 Cyclic voltammograms for the first 8 cycles of Li-S<sub>1</sub>NDI<sub>85</sub> and Li-S<sub>2</sub>NDI<sub>72</sub> half-cells. The cut-off voltage range was 1.7 V to 3.0 V for the S<sub>1</sub>NDI<sub>85</sub>, and 1.6 V to 2.8 V for the S<sub>2</sub>NDI<sub>72</sub> cell. CV was performed with a scan rate of 0.1 mV s<sup>-1</sup> for both cells.

and 2.5 V. These redox pairs are similar to the redox features of the cross-linker NDI-pro, shown by Matsidik *et al.*, yet they show differences also regarding the exact shape. It remains unclear whether the change is influenced by active sulfur or solely by the modified structure with broken allyl bonds in the polymer network.

In comparison, the first CV cycle of S<sub>2</sub>NDI<sub>72</sub> features significant currents for charging at 2.3 V and discharging at 2.0 V, *i.e.* at lower potentials than the NDI-pro double redox pair. Especially the latter forms a clear signature of active sulfur whereas the peak at 2.7 V still suggests redox activity of the NDI.

Over the following cycles, the cyclic voltammogram of S<sub>2</sub>NDI<sub>72</sub> gradually changes. The additional charging peak at 2.3 V decreases, whereas the peaks at 2.5 V and 2.7 V increase. Accordingly, the discharge peaks at 2.3 V and 2.5 V increase. The voltage of the discharge peak at 2.0 V shifts to 1.95 V towards cycle number 5. Beginning with the 6th cycle, one more peak just below 1.8 V appears which can be assigned to the decomposition of LiNO<sub>3</sub>.<sup>40</sup> The specific capacity increases from 110 mAh g<sup>-1</sup> to over 140 mAh g<sup>-1</sup> but already starts to decrease within the first 10 cycles.

The cycling of S<sub>1</sub>NDI<sub>85</sub> is significantly more stable. The charging and discharging peaks barely shift their voltages. However, their currents increase which corresponds to an increasing specific capacity, from 55 mAh g<sup>-1</sup> to 70 mAh g<sup>-1</sup>. Recent studies<sup>19</sup> show that the maximal specific capacity of this cell type is reached after *ca.* 300 cycles which was not investigated here. However, the lower specific capacity compared to

S<sub>2</sub>NDI<sub>72</sub> suggests that there is less electrochemically active sulfur contributing in S<sub>1</sub>NDI<sub>85</sub>.

Because of the complexity of the S<sub>n</sub>NDI<sub>y</sub> systems and changing redox potentials compared to their precursors, it is challenging to perform a quantitative analysis of electrochemically active components or the distribution of sulfur species in the polymer network from cyclic voltammograms. Therefore, operando NEXAFS spectra have been measured during cycling as a method that allows for quantification by investigating electronic states of sulfur dynamically.

### 3.2 Operando NEXAFS measurements

NEXAFS spectra of Li-S<sub>1</sub>NDI<sub>85</sub> and Li-S<sub>2</sub>NDI<sub>72</sub> battery half-cells were recorded in various states of charge during cyclic voltammetry. In Fig. 5, the spectra of both cells in fully charged and

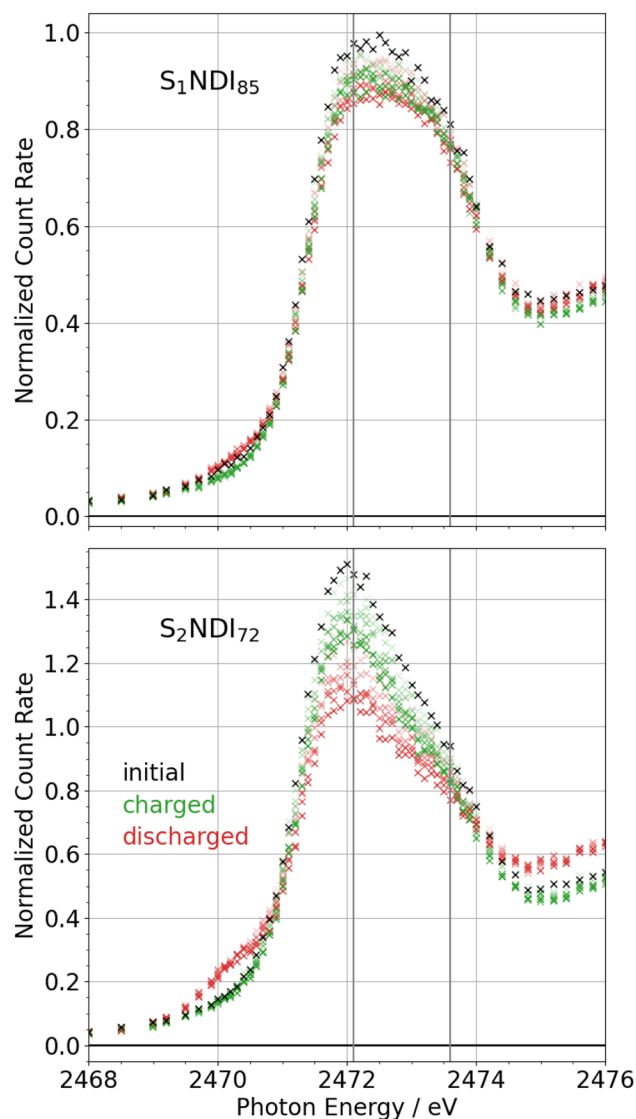


Fig. 5 Operando NEXAFS spectra of Li-S<sub>1</sub>NDI<sub>85</sub> and Li-S<sub>2</sub>NDI<sub>72</sub> half-cells, taken initially before cycling (black), in fully charged (green) and fully discharged (red) states, respectively. Early cycles are plotted more transparent than later cycles.



discharged states are shown. There are three significant findings that can be concluded from a qualitative analysis. Firstly, there are deviations in the spectral shape in the energy range of 2472 eV to 2474 eV which is determined by elemental sulfur and how it is incorporated into the  $S_n\text{NDI}_y$  network. In the  $S_2\text{NDI}_{72}$ , the peak at 2472 eV is more intense which indicates the presence of longer sulfur strands,<sup>34</sup> whereas the broader shape in  $S_1\text{NDI}_{85}$  suggests the existence of several shorter sulfur strands. Secondly, the variance between charged and discharged spectra, both in the range of neutral sulfur and for the lithium polysulfide signal at 2470 eV, is larger in the  $S_2\text{NDI}_{72}$  which shows that a larger amount of sulfur is electrochemically active during cycling, compared to  $S_1\text{NDI}_{85}$ . For  $S_2\text{NDI}_{72}$ , there is even a significant amount of sulfur cycling in the energy range of 2475 eV to 2477 eV (see Fig. 2) which can be assigned to the (reversible) formation and deformation of lithium monosulfide ( $\text{Li}_2\text{S}$ ).<sup>4,15</sup> Thirdly, over the course of several cycles, the total signal of the neutral sulfur is decreasing in both cells, with this effect being stronger in  $S_2\text{NDI}_{72}$  as well. This indicates irreversible processes including the loss of active S-strand material and thus capacity fading.

The two latter observations are in line with the CV profiles where  $S_2\text{NDI}_{72}$  has higher currents (and thus higher capacities, indicating a higher amount of active sulfur) and a larger value of and more significant changes to the electro-active potentials (as a sign of loss of active material).

A quantitative analysis of the sulfur strand lengths in the cathode may reveal a more detailed correlation between the polymer structure and the electrochemical properties of the batteries, *i.e.* which sulfur strands contribute to the loss of active material and which are stable during cycling.

### 3.3 Evolution of sulfur strand length distribution during cycling

Each of the operando NEXAFS spectra can be analyzed regarding the composition of sulfur species. By a linear combination analysis, the distribution of sulfur strand lengths in the organo-sulfur network and relative amounts of lithium sulfur (LiS) bonds in the cathode can be quantitatively determined. The evolution of the respective molar fractions and the LiS coefficient during cycling is shown in Fig. 6.

In  $S_1\text{NDI}_{85}$ , the molar fractions of mono-, di- and trisulfide strands vary within a certain range, mainly between 0.10 and 0.18 for all of these species. The standard uncertainty of the molar fraction resulting from the fitting is typically 0.04 for di- and trisulfides and less than half the value for monosulfides. A systematic trend of the distribution of sulfur strand lengths higher than this uncertainty cannot be identified. Relatively high random deviations and an anti-correlation between the trisulfide and the mono- and disulfide molar fractions are observable. This can be explained by the constraint that all molar fractions sum to 1 before the renormalization of the spectrum. Since all molar fractions are relatively low and have similar values, the fitting result seems to be less significant.

Only the LiS signal cycles as it reaches its maximum in the fully discharged state and almost vanishes when the battery is

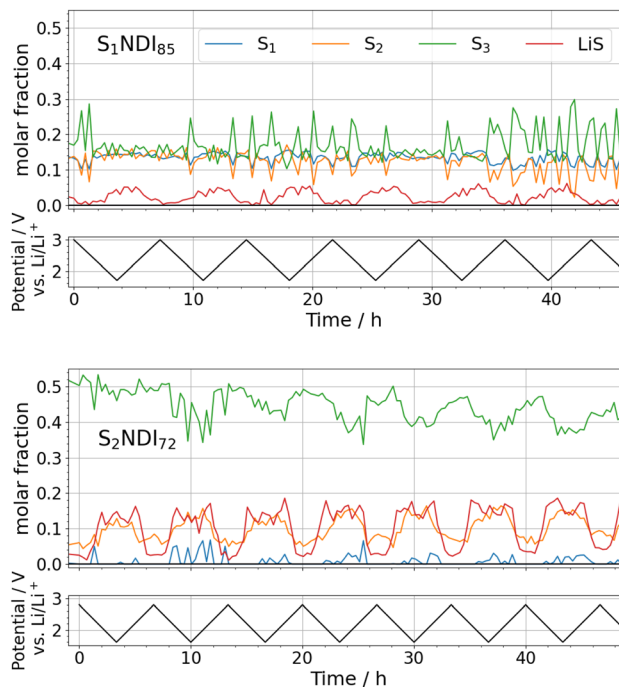


Fig. 6 Evolution of molar fractions of different sulfur strand lengths and of the signal of lithium sulfur bonds (LiS) over several CV cycles, determined by a linear combination analysis of operando NEXAFS spectra of  $\text{Li}-S_1\text{NDI}_{85}$  and  $\text{Li}-S_2\text{NDI}_{72}$  half-cells.  $S_1$ ,  $S_2$  and  $S_3$  species are represented by DPS, DPDS and DMTS basis spectra and correspond to molar fractions of sulfur in mono-, di- and trisulfide strands, respectively. The LiS coefficient is proportional, but not equal to the molar fraction of lithium sulfur bonds.

fully charged. The main formation of lithium sulfur bonds happens at potentials of around 2.0 V where the CV curves do not show a peak. Similar considerations apply for the deformation of LiS bonds at a charging potential of around 2.3 V. Nevertheless, and although the maximum LiS signal is relatively low, this means that there is a significant amount of sulfur electrochemically active during cycling and therefore contributing to the battery's capacity. The amplitude of this LiS signal does not change over the course of several cycles, indicating that the process is reversible. Remarkably, the LiS coefficient does not show any anti-correlation with the polysulfides which makes its evolution significant despite its low amplitude of around 0.05 and a standard fitting uncertainty of 0.02. Due to the poor sensitivity in the evolution of the polysulfide molar fractions, it cannot be concluded where the active sulfur contributing to the LiS signal is incorporated into the cathodic polymer network.

All components of the  $S_2\text{NDI}_{72}$  cycle synchronously with the CV curve. The molar fraction of trisulfides, the fitted species with the longest sulfur strand length, decreases during discharging, while that of the shorter sulfur strands increases together with the signal of lithium sulfur bonds. Although the  $S_2$  and LiS coefficients cannot be compared on an absolute scale, they are synchronously increasing during discharging and decreasing during charging. This opposite behaviour of the



cycling molar fractions of  $S_3$  compared to  $S_2$  and LiS suggests that long sulfur strands break into shorter strands while building lithium sulfur bonds. Remarkably, the  $S_3$  molar fraction increases again during recharging and shows a certain level of reversibility, even though it does not fully regain its original level. The sulfur strand lengths in the copolymer can be reduced by the formation of lithium polysulfides ( $Li_2S_x$ ,  $x \geq 2$ ). Alternatively, as indicated by the reversibility of the  $S_2$  and  $S_3$  signals, lithium can also covalently bond to the sulfur in the polymer network to form  $R-CH_2-S_x-Li$  groups.

The expected S K-edge spectra of  $Li_2S_2$  and  $CH_3SLi$  obtained from simulation are shown in Fig. 7. The  $Li_2S_2$  spectrum has a single sharp peak at approximately 2470 eV, along with some weaker resonances centered around 2474 eV, which is in good agreement with previous simulations.<sup>29</sup> The  $CH_3SLi$  spectrum shows two main peaks, one weaker peak at approximately 2470.8 eV and a second stronger peak at around 2472.5 eV. The spectral signature of  $CH_3SLi$  therefore resembles a spectrum of a neutral sulfur species with a contribution of a LiS peak, yet with a slightly shifted energy axis. A correlating evolution of  $S_2$  and LiS molar fractions therefore indicates the presence of lithium thiolate groups which are thought to be stable.

The lithium sulfur bonds form at around 2.3 V, *i.e.* at higher discharge potentials than in  $S_1NDI_{85}$ . While this could indicate that there are additional electrochemical potentials where sulfur contributes to the specific capacity in  $S_2NDI_{72}$ , the potential can also be shifted because of an interaction between

sulfur and NDI. The formation of  $R-CH_2-S_x-Li$  groups can also influence the electrochemical potentials in the battery.

The molar fraction of  $S_1$  only gives non-zero values close to the fully discharged state. Hence, it is possible for monosulfide strands to build, but they disappear again fully in the charging process. The monosulfide linkages form at lower potentials than LiS bonds and are thus created in a separate process. However, monothioethers are not thought to be electrochemically active themselves. Note that lithium monosulfide ( $Li_2S$ ) is present in the spectra. However, since its resonances are not inside of the selected fitting energy range, its molar fractions were not quantified here.

The voltage region where LiS bonds are built in  $S_2NDI_{72}$  lies between 2.4 V and 2.0 V, *i.e.* in the range of the broad discharge plateau in its CV curves. In contrast to the CV curves and NEXAFS spectra of  $S_1NDI_{85}$ , the voltage region of the discharge plateau is shifted and the changing LiS coefficient shows a clear correlation with  $S_2$  and anticorrelation with  $S_3$  molar fractions. Thus, Li seems to bond to single sulfur atoms attached to the polymer network in  $S_1NDI_{85}$ , whereas different reactions happen in  $S_2NDI_{72}$ . Besides the formation of lithium polysulfides, lithium covalently bonding to sulfur in the network while shortening sulfur strands can contribute to the electrochemical activity. Similar considerations apply for the charging plateau between 2.3 V and 2.6 V, where these simultaneously occurring (and competing) processes are reversed.

Over the course of several cycles, the molar fraction of trisulfide strands decreases gradually. This suggests that sulfur strands consisting of at least 3 sulfur atoms partially undergo irreversible conversion processes which lead to loss of active material. On the other hand, the amplitude of  $S_1$  and  $S_2$  molar fractions tends to increase together with the coefficient representing LiS bonds, while the minima of the LiS molar fraction for charged states slightly increase. In the CV curves, the lowest voltage potentials, namely at 2.0 V during discharging and especially at 2.3 V during charging, have a decreasing intensity, whereas the currents of the other CV peaks as well as the capacities of the batteries increase during the first few cycles. This opposite electrochemical behaviour can be linked to the molar fractions of sulfur species where LiS bonds, especially involving longer sulfur strands represented by  $S_3$ , have a decreasing contribution to the capacity. On the other hand, shorter sulfur strands build and rebuild reversibly during cycling and are additionally formed from broken, originally longer strands. Thus, these irreversible processes appear to be inherent to the chemical structure of the organo-sulfur networks used here.

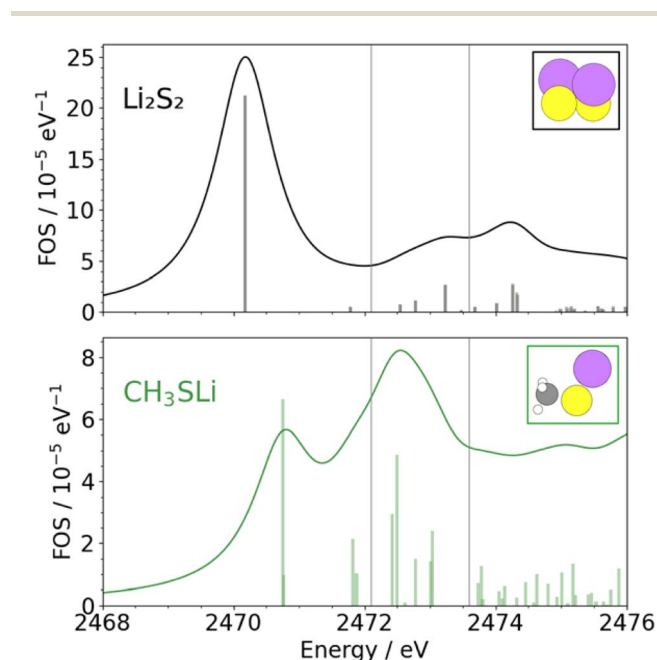


Fig. 7 Theoretical NEXAFS spectra of  $Li_2S_2$  and  $CH_3SLi$  in a 1,2-dimethoxyethane/1,3-dioxolane (DME/DOL) solvent environment. The inset shows a 3D representation of each molecule where lithium (Li) atoms are depicted in purple, sulfur (S) in yellow, carbon (C) in gray, and hydrogen (H) in white. A stick spectrum represents the oscillator strength of each transition, and the folded oscillator strengths (FOS) are obtained by folding the stick spectrum with a Lorentzian profile with a full width at half maximum of  $2\gamma = 1.1$  eV.

## Conclusion

Using a quantitative, self-absorption corrected linear combination analysis of operando NEXAFS spectra, it was shown how the molar fractions of different sulfur species in lithium organo-sulfur batteries evolve during several discharge-charge cycles. Mono- and disulfide strands are found to be stable or undergo reversible processes whereas sulfur originating from longer strands partially gets lost from the cathode irreversibly. This



explains why batteries with lower sulfur load have a superior cycle stability due to their shorter sulfur strands.

Electrochemically, monothioethers are not active and thus do not contribute to the specific capacity of the battery. Thus, the ideal structure for organo-sulfur cathode materials consists of disulfide strands. However, their contribution to the capacity remains unclear and can only be evaluated for networks with a significantly higher molar fraction of disulfide linkages with absent species of longer strands.

From our present perspective we anticipate that the synthesis of chemically distinct species, *i.e.* a maximised content of disulfide strands, has been unsuccessful in our hands and is at least very challenging using inverse vulcanization with elementary S<sub>8</sub>.<sup>25</sup> Whether modified synthetic protocols are suited to come closer to such structure remains an open question.

In the described networks, the sulfur strands are coupled with the polymer backbone and thus determine the polymer structure depending on the sulfur strand length distribution. An alternative approach could be to decouple the sulfur chemistry from the network chemistry and install disulfides in other forms or organic cathodes. This would also leave the organo (network) structure unchanged during cycling.

Overall, operando quantification has enabled unique mechanistic insight into the electrochemical processes during charge–discharge cycles of lithium organosulfur batteries, which are challenging to capture using other techniques.

## Author contributions

RM synthesized the material. KS and RM prepared the samples. NEXAFS measurements were performed by KS and MM, and analyzed together with HY. AG calculated theoretic NEXAFS spectra. MM, MW and MS designed the full project and all authors participated in writing.

## Conflicts of interest

There are no conflicts of interest to declare.

## Data availability

Data for this article, including all presented experimental NEXAFS spectra and CV data, are available in the Open Access Repository of the Physikalisch-Technische Bundesanstalt (PTB-OAR) at <https://doi.org/10.7795/720.20250710>.<sup>26</sup>

## Acknowledgements

We acknowledge funding by the German Research Foundation (DFG) through the Priority Programme “Polymer-based Batteries” (SPP 2248) under project number 441323218.

## Notes and references

1 U. Herbert, Electric dry cells and storage batteries, *US Pat.*, US3043896A, 1962.

- 2 A. Manthiram, S.-H. Chung and C. Zu, *Adv. Mater.*, 2015, **27**, 1980–2006.
- 3 Y. V. Mikhaylik and J. R. Akridge, *J. Electrochem. Soc.*, 2004, **151**, A1969.
- 4 Y. Gorlin, M. U. Patel, A. Freiberg, Q. He, M. Piana, M. Tromp and H. A. Gasteiger, *J. Electrochem. Soc.*, 2016, **163**, A930.
- 5 L. Zhang and J. Guo, *Arabian J. Sci. Eng.*, 2019, **44**, 6217–6229.
- 6 Y. Huang, L. Lin, C. Zhang, L. Liu, Y. Li, Z. Qiao, J. Lin, Q. Wei, L. Wang, Q. Xie, *et al.*, *Adv. Sci.*, 2022, **9**, 2106004.
- 7 W. Qiu, C. An, Y. Yan, J. Xu, Z. Zhang, W. Guo, Z. Wang, Z. Zheng, Z. Wang, Q. Deng, *et al.*, *J. Power Sources*, 2019, **423**, 98–105.
- 8 S. Bai, X. Liu, K. Zhu, S. Wu and H. Zhou, *Nat. Energy*, 2016, **1**, 1–6.
- 9 Y. Zhang, C. Guo, L. Zhou, X. Yao, Y. Yang, H. Zhuang, Y.-R. Wang, Q. Huang, Y. Chen, S.-L. Li, *et al.*, *Small Sci.*, 2023, **3**, 2300056.
- 10 Y. Fan, Z. Niu, F. Zhang, R. Zhang, Y. Zhao and G. Lu, *ACS Omega*, 2019, **4**, 10328–10335.
- 11 Y. Liu, Y. Elias, J. Meng, D. Aurbach, R. Zou, D. Xia and Q. Pang, *Joule*, 2021, **5**, 2323–2364.
- 12 K. Liu, H. Zhao, D. Ye and J. Zhang, *Chem. Eng. J.*, 2021, **417**, 129309.
- 13 R. Fang, H. Xu, B. Xu, X. Li, Y. Li and J. B. Goodenough, *Adv. Funct. Mater.*, 2021, **31**, 2001812.
- 14 S. Muduli, J. M. Blázquez-Moreno, A. Benítez and M. R. Buchmeiser, *Appl. Energy*, 2025, **389**, 125778.
- 15 R. Dominko, A. Vizintin, G. Aquilanti, L. Stievano, M. J. Helen, A. R. Munnangi, M. Fichtner and I. Arcon, *J. Electrochem. Soc.*, 2017, **165**, A5014.
- 16 N. Goujon, N. Casado, N. Patil, R. Marcilla and D. Mecerreyes, *Prog. Polym. Sci.*, 2021, **122**, 101449.
- 17 B. Esser, F. Dolhem, M. Becuwe, P. Poizot, A. Vlad and D. Brandell, *J. Power Sources*, 2021, **482**, 228814.
- 18 Y. Lu and J. Chen, *Nat. Rev. Chem.*, 2020, **4**, 127–142.
- 19 R. Matsidik, K. Skudler, S. de Kock, A. Seifert, M. Müller, M. Walter, S. Choudhury and M. Sommer, *ACS Appl. Energy Mater.*, 2023, **6**, 9466–9474.
- 20 A. Hoefling, D. T. Nguyen, P. Partovi-Azar, D. Sebastiani, P. Theato, S.-W. Song and Y. J. Lee, *Chem. Mater.*, 2018, **30**, 2915–2923.
- 21 S. Haldar, P. Bhauriyal, A. R. Ramuglia, A. H. Khan, S. De Kock, A. Hazra, V. Bon, D. L. Pastoetter, S. Kirchhoff, L. Shupletsov, *et al.*, *Adv. Mater.*, 2023, **35**, 2210151.
- 22 M. Wu, Y. Cui, A. Bhargav, Y. Losovyj, A. Siegel, M. Agarwal, Y. Ma and Y. Fu, *Angew. Chem., Int. Ed.*, 2016, **55**, 10027–10031.
- 23 A. Rafie, R. Pereira, A. A. Shamsabadi and V. Kalra, *J. Phys. Chem. C*, 2022, **126**, 12327–12338.
- 24 J. Stöhr, *NEXAFS Spectroscopy*, Springer Science & Business Media, 2013, vol. 25.
- 25 K. Skudler, R. Matsidik, H. Yang, M. Walter, M. Sommer and M. Müller, *J. Anal. At. Spectrom.*, 2025, DOI: [10.1039/D5JA00269A](https://doi.org/10.1039/D5JA00269A).
- 26 K. Skudler, H. Yang, R. Matsidik and M. Müller, *Ex Situ and Operando NEXAFS Spectra of Organo-Sulfur Compounds*, 2025, DOI: [10.7795/720.20250710](https://doi.org/10.7795/720.20250710).



- 27 M. Krumrey and G. Ulm, *Nucl. Instrum. Methods Phys. Res., Sect. A*, 2001, **467**, 1175–1178.
- 28 C. Zech, P. Hönicke, Y. Kayser, S. Risse, O. Grätz, M. Stamm and B. Beckhoff, *J. Mater. Chem. A*, 2021, **9**, 10231–10239.
- 29 T. A. Pascal, K. H. Wujcik, J. Velasco-Velez, C. Wu, A. A. Teran, M. Kapilashrami, J. Cabana, J. Guo, M. Salmeron, N. Balsara, *et al.*, *J. Phys. Chem. Lett.*, 2014, **5**, 1547–1551.
- 30 K. Skudler, M. Walter, M. Sommer and M. Müller, *J. Anal. At. Spectrom.*, 2024, **39**, 2893–2902.
- 31 J. Enkovaara, C. Rostgaard, J. J. Mortensen, J. Chen, M. Dulak, L. Ferrighi, J. Gavnholt, C. Glinsvad, V. Haikola, H. A. Hansen, *et al.*, *J. Phys. Condens. Matter*, 2010, **22**, 253202.
- 32 A. Nilsson and L. G. M. Pettersson, *Surf. Sci. Rep.*, 2004, **55**, 49–167.
- 33 L. Triguero, L. Pettersson and H. Ågren, *Phys. Rev. B: Condens. Matter Mater. Phys.*, 1998, **58**, 8097.
- 34 S. de Kock, K. Skudler, R. Matsidik, M. Sommer, M. Müller and M. Walter, *Phys. Chem. Chem. Phys.*, 2023, **25**, 20395–20404.
- 35 J. P. Perdew, K. Burke and M. Ernzerhof, *Phys. Rev. Lett.*, 1996, **77**, 3865.
- 36 A. Held and M. Walter, *J. Chem. Phys.*, 2014, **141**, 174108.
- 37 C. V. Pham, L. Liu, B. Britton, M. Walter, S. Holdcroft and S. Thiele, *Sustain. Energy Fuels*, 2020, **4**, 1180–1190.
- 38 M. Ljungberg, J. J. Mortensen and L. Pettersson, *J. Electron Spectrosc. Relat. Phenom.*, 2011, **184**, 427–439.
- 39 E. A. B. Johnsen, N. Horiuchi, T. Susi and M. Walter, Explicit core-hole single-particle methods for L- and M- edge X-ray absorption and electron energy-loss spectra, *arXiv*, preprint, arXiv:2504.08458, 2025, DOI: [10.48550/2504.08458](https://doi.org/10.48550/2504.08458).
- 40 F. C. de Godoi, D.-W. Wang, Q. Zeng, K.-H. Wu and I. R. Gentle, *J. Power Sources*, 2015, **288**, 13–19.

